STATOR-ROTOR INTERACTION IN THE TIP LEAKAGE FLOW OF AN INLET VANED LOW-SPEED AXIAL FAN

ABSTRACT

Purpose

The purpose of the paper is to quantify the impact of the non-uniform flow generated by the upstream stator on the generation and convection of the tip leakage flow structures in the passages of the rotor blades in a low-speed axial fan.

Design/Methodology/Approach

A full 3D-viscous Unsteady RANS (URANS) simulation of the flow within a periodic domain of the axial stage has been performed at three different flow rate coefficients (ϕ=0.38, 0.32, 0.27) using RNG k-ε turbulence modelling. A typical tip clearance of 2.3% of the blade span has been modelled on a reduced domain comprising a 3-vaned stator and a 2-bladed rotor with circumferential periodicity. A non-conformal grid with hybrid meshing, locally-refined O-meshes on both blades and vanes walls with [100x25x80] elements, a 15-node meshed tip gap and circumferential interfaces for sliding mesh computations were also implemented. The unsteady motion of the rotor has been covered with 60 time steps per blade event. The simulations were validated with experimental measurements of the static pressure in the shroud of the blade tip region.

Findings

It has been observed that both tip leakage flows (TLF) and intensities of the tip leakage vortex (TLV) are significantly influenced by upstream stator wakes, especially at nominal and partial load conditions. In particular, the leakage flow, which represents 12.4% and 11.3% of the working flow rate respectively, has shown a clear periodic fluctuation clocked with the vane passing period in the relative domain. The periodic fluctuation of the TLF is in the range between 2.8% and 3.4% of the mean value. In addition, the trajectory of the tip vortex is also notably perturbed, with RMS fluctuations reaching up to 18% and 6% in the regions of maximum interaction at 50% and 25% of the blade chord for nominal and partial load conditions, respectively. On the contrary, the massive flow separation observed in the tip region of the blades for near-stall conditions prevents the formation of TLV structures and neglects any further interaction with the upstream vanes.

Research limitations/Implications

Despite the increasing use of LES modelling in turbomachinery environments, which requires extremely high computational costs, URANS modelling is still revealed as a useful technique to describe highly-complex viscous mechanisms in 3D swirl flows, such as unsteady tip flow structures, with reasonable accuracy.

Originality/Value

The paper presents a validated numerical model that simulates the unsteady response of the TLF to upstream perturbations in an axial fan stage. It also provides levels of instabilities in the TLV derived from the deterministic non-uniformities associated to the vane wakes.

Keywords: Stator-Rotor interaction, tip clearance, tip leakage flow, tip vortex, deterministic stresses, axial fan.

1. INTRODUCTION

The tip leakage flow and the generation of the tip vortex in the tip clearance of axial turbomachinery is a highly-3D, unsteady viscous phenomenon that generates volumetric losses and induces a detrimental impact on machine performance (Venter and Kröger, 1992; Denton, 1993). It arises due to the generation of a high-velocity jet across the tip gap, that it is driven due to pressure difference in both side of the blades, and evolves streamwise rolling-up into a tip vortex. In the case of low-speed axial fans, the driving forces are not so intense so the clearance is usually enlarged in order not to compromise the mechanical integrity of the rotors. However, despite of its moderate intensity, it may present a significant impact on the flow structures in the outer half of the rotor passages.

The structure of the tip vortex is locked on the blade-to-blade patterns on the flow, following a predictable trajectory in the relative frame of reference. In the case of multistage environment, the presence of stator vanes generates a non-uniform flow at the inlet of the moving row, thus imposing a tangential pressure gradient for the tip leakage flow. Consequently, deterministic interactions between the stator flow structures and the tip leakage may arise, having an impact on the stability of the tip vortex. Currently, few works have addressed the deterministic contribution of upstream non-uniformities on the tip leakage flow, so more investigation is needed to understand the complexity of these unsteady mechanisms.

The relevance of the tip vortex structures in the flow passages of axial rotors has been analyzed using both numerical and experimental methodologies. Pioneering experimental investigations used intrusive probes, despite of the inherent difficulty of characterizing the flow in the rotor frame with a rotating measuring system (Storer and Cumptsy, 1991; Lakshminarayana *et al.*, 1995; Jang *et al.*, 2005). In addition, the extremely reduced gaps were a serious handicap for the development of reliable and practicable sensors. Recent investigations have employed PIV systems to identify and track the evolution of tip vortex structures in axial turbomachinery (Jin *et al.*, 2011; Miorini *et al.*, 2012; Lee *et al.*, 2019). These investigations have reported notable findings, highlighting the physical mechanisms behind the mixing out of the tip leakage flow and analyzing the impact of different parameters, especially the size of the tip gap and the inclusion of tip plates to control the leakage flow (Bae *et al.*, 2005; Aktürk and Camci, 2010; Corsini *et al.*, 2010).

Concerning numerical methodologies, the complexity of these internal flows and the large number of blade and vane passages involved requiring extremely high-density meshes in small gaps has conditioned severely the use of these techniques in the last decades (Van Zante *et al.*, 2000; Borello *et al.*, 2007). Initial investigations employed RANS computations providing encouraging predictions of the tip vortex trajectories with relatively coarse meshes (Inoue and Furukawa, 2002; Lee *et al.*, 2003; Zhu *et al.*, 2005, Fernández Oro *et al.*, 2009) for rotor-only fans. With the increasing computational capacities in recent years (aka. *High-Performance Computing*), different research groups

have explored the use of Scale-Resolving Simulations (SRS) to simulate tip leakage flows in single rows (Pogorelov *et al.*, 2016; Ye *et al*., 2017; Park *et al.*, 2019; Moghadam *et al.*, 2019). In particular, LES-based simulations with restrictions for wall-modelling (zonal RANS) have been employed to describe all-range scales associated to the tip vortex with high fidelity in low-speed axial fans. Other authors have employed LES techniques to simulate one stage and a half of an axial compressor, but with a number of nodes extremely prohibitive for industrial purposes (Hah *et al.*, 2015).

Since the number of nodes required for LES simulation of stator-rotor configurations with tip clearance modelling is significantly high (up to several dozens of million cells), Unsteady RANS (URANS) modelling is still being used by a number of researchers as a useful approach, with an acceptable compromise between accuracy and computational cost. Effectively, recent investigations have provided valuable information, showing that it is feasible to accurately simulate these three-dimensional, vortical structures using URANS modelling (Zhang *et al.*, 2015; Jung and Joo, 2018; Mao *et al.*, 2019). Moreover, when the full-unsteady sliding mesh technique is employed in multistage environments, the URANS approach turns to be the more realistic and practicable option.

Consequently, the current state-of-the-art with respect to numerical modelling of the tip leakage flow in axial fans is rapidly evolving towards the use of LES techniques for a high-fidelity description of the flow structures. However, systematic studies modifying different flow parameters at the same time (tip clearances, interrow gaps, solidities, flow rate conditions…) are still not really affordable due to the extraordinary high computational costs associated, being more evident in case of multistage configurations. Obviously, LES modelling will become the standard for these numerical studies in recent years, substituting URANS techniques even for the analysis of complex, 3D turbomachinery flows at an industrial level (typically for engineering quantification, characterization and further optimization); but in the meantime, URANS still appears as the most convenient numerical tool to analyze basic flow features and overall trends at a time-resolved level for secondary flows in multistage axial fans.

The objective of the present paper is the analysis of the deterministic interaction established between the stator wakes and the tip leakage flow in a single-stage, low-speed axial fan. Special attention is devoted to the unsteady evolution of the tip leakage structures in the rotor passages in the relative frame of reference and how it is influenced by the operating flow rate of the fan. A full unsteady RANS simulation, taking advantage of a well-established sliding mesh technique employed previously by the authors (Fernández Oro *et al.*, 2019), has been adopted to describe accurately the blade passing frequencies of the fan. The numerical model has been validated with global variables for the performance curves and also with local measurements in the tip region to characterize the wall pressure fluctuations. In addition, variations over the mean-time structures will be shown to provide levels and distributions of instabilities induced on the tip leakage flow by the upstream stator. The instantaneous tip leakage flow for the blades will be computed and studied for different flow rate conditions. The final objective is to provide levels of instabilities in the tip vortex derived from deterministic non-uniformities associated with vane-to-vane flow patterns, applicable for further modelling of deterministic stresses.

2. LOW-SPEED AXIAL FAN: GEOMETRY, OPERATING PARAMETERS AND WALL-PRESSURE MEASUREMENTS

A single-stage low-speed axial fan with a Stator-Rotor configuration is considered in the present study (Figure 1). The stator (S) is composed of 13 inlet guide vanes based on the British circular profile C1. The rotor (R) comprises 9 blades based on the NACA 65-012 airfoil and is radially twisted to provide a free-vortex velocity distribution at the outlet. The hub and tip diameters of the fan are 380 and 820 mm respectively, with a 5-mm tip clearance for the rotor that represents 2.3% of the blade span. The axial distance between vanes and blades is 50 mm. The rotational speed of the fan is 2400 rpm. Table 1 summarizes the basic geometrical data and operating parameters at the tip. More details of the axial fan can be found in Fernández Oro *et al*. (2007, 2011).

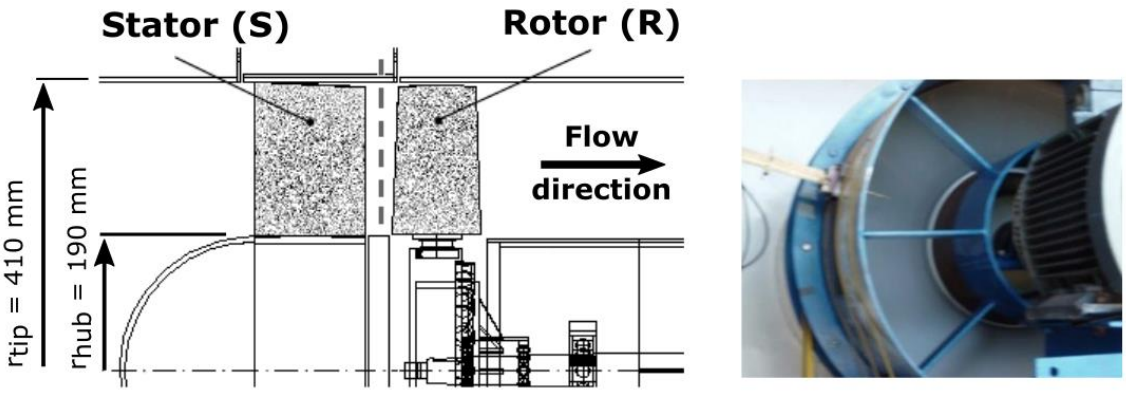

Figure 1. Sketch of the Stator-Rotor configuration (left drawing) of the low-speed axial fan (running in the experimental facility, right image).

Table 1. Geometrical data and operating parameters at the tip.

Tip geometry	Stator	Rotor
Number of vanes/blades	13	9
Chord length, c (mm)	170.8	157.4
Pitch length, p (mm)	198.1	286.2
Stagger angle (deg)	10.8	66.5
Thickness-to-chord ratio (%)	3.0	8.0
Camber angle (deg)	23.3	5.7
Tip clearance (mm)	-	5
Tip velocity (m/s)	-	103.1

The axial fan has been operated in a standardized fan test rig (developed according to British Standards BS848 for type A tests – Methods of Testing Performance), which has been used for intensive hot-wire measurements in previous investigations. The facility has been used to obtain the flow description in the axial stage for different operating conditions, including the nominal flow rate (Q_N=16.5 m^3/s), partial off-design rate (85%Q_N) and off-design near-stall rate (70%Q_N).

For the present investigation, the static pressure information on the casing wall near the blade tip was acquired to investigate the unsteady characteristics of the tip-leakage flow. Piezoelectric pressure transducers (Kistler 7031, with an operational range between 0 to 2.5 bar and a <1% FOS uncertainty) were embedded in pin-holes on the casing wall near the blade tip, at an axial distance corresponding to the midchord of the rotor blades (s/c=0.5). To increase the signal-to-noise ratio, a capacitive amplifier (Kistler Charge Amplifier Type 5011B) was introduced (see figure 2) to convert the outlet signal of the transducer into a proportional voltage signal, with a typical amplification of 0.1 bar/V for a 2.5 V FS. Hence, the fan rotor casing was instrumented with 15 inserts along the circumferential direction corresponding to the pitch of the vanes. Special care was done to assure that the transducers were mounted flushed with the casing inner wall, according to Sheard *et al*. (2011). The measurements were recorded at a sampling rate of 36 kHz (far beyond the Nyquist limit of the maximum frequency response of the sensor, up to 120 kHz), and the instantaneous signals were low-pass filtered using a typical 5th-order Butterworth filter with a 7.2 kHz cut-off frequency. With this value, small-scale turbulent motion is removed while periodic, unsteady fluctuations related to the blades motion are preserved during signal preconditioning. Preliminary tests concluded that 20 times the BPF is a reasonable selection for the present database. Additionally, the measurements were phase-averaged to ensure that all the turbulent scales are decoupled from deterministic motions, so the periodic (deterministic) unsteady response of the pressure in the tip gap is finally obtained. A signal from a shaft encoder –optical trigger– is typically used for synchronizing the sensor time series with the phase of the machine. Figure 2 shows the experimental setup and a schematic diagram of the measuring system.

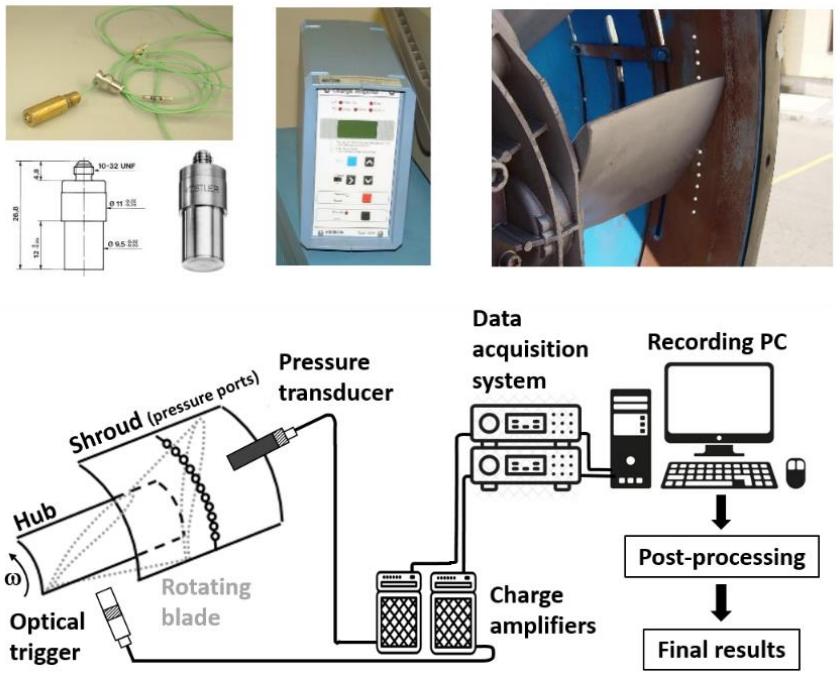

Figure 2. Wall-pressure measurements: equipment set-up (top) and schematic diagram (bottom)

3. NUMERICAL METHODOLOGY AND URANS COMPUTATIONS

Currently, LES and hybrid RANS-LES are becoming a feasible option to simulate the turbulent flow inside multistage turbomachinery. Moreover, a significant number of references can be found in the scientific literature concerning the use of these techniques to simulate the viscous flow in the tip gap. Unfortunately, in the case of tip-leakage modelling, the grid requirements are dramatically increased, within the range of 10^7 cells for wall-modelled computations and even 10^8 in case of wall-resolving meshes. High-Performance Computing, which it is not always available for researchers, is thus essential to obtain good results in a reasonable period of time. To overcome this problem, URANS modelling with enhanced wall treatment has been still considered as a valid approach to study the basic features of the flow structures associated with the tip leakage flow. In accordance with recent contributions to the literature, in which RANS modelling is still used (Zhang *et al.*, 2015; Jung and Joo, 2018; Mao *et al.*, 2019), this work reveals that present computations (validated in section 3.5) provide a correct picture of the tip vortex motion in this axial fan.

3.1. Numerical model and solver

The full 3D model of the fan, using the sliding mesh technique, has been implemented in the ANSYS-FLUENT® v16.2 solver to resolve the Unsteady RANS equations assuming incompressible, viscous flow of a single-phase Newtonian fluid (air):

- Continuity equation:

$$\frac{\partial \bar{u}_i}{\partial x_i} = 0 \tag{1}$$

- Momentum equation:

$$\rho \frac{\partial \bar{u}_i}{\partial t} + \rho \frac{\partial (\bar{u}_i \bar{u}_j)}{\partial x_j} = -\frac{\partial \bar{p}}{\partial x_i} + \mu \nabla^2 \bar{u}_i + \frac{\partial \tau_{ij}}{\partial x_j} \tag{2}$$

This set of equations has been discretized with the Finite Volume Methodology using a higher-order differencing scheme (QUICK) for the spatial convective terms. The Green-Gauss cell-based method has been used for the computation of the spatial gradients over the diffusion terms in the momentum equation. Also, a second-order discretization has been employed for the transport equations of the turbulent equations (see section 3.3). The temporal discretization for the unsteady term has been also fixed to second-order. A segregated solver with the PISO algorithm has demonstrated an accurate compromise between stability and CPU time.

To reduce the computational costs, a circumferential periodicity has been assumed such that the flow over only two blade passages is computed in this study (Figure 3). As a consequence, since the original blade/vane count ratio is 9:13, a slight modification in the stator pitch was introduced to match an exact 2:3 proportion. The pitch modification of the stator vane row is around a 3%, which has been considered negligible for this kind of turbomachines (Arnone *et al.*, 2004). Two interfaces are also introduced to allow the relative angular motion of the rotor domain within the sliding mesh technique. The rotating mesh of the rotor provides a full-unsteady simulation taking into account the

changes in the relative positions of the moving and fixed rows over time. In addition, the numerical domain was extended one blade chord upstream and three blade chords downstream to guarantee independency with respect to inlet/outlet conditions. Complementarily, seven transversal planes covering the chord of the blades at the tip in the streamwise direction have been defined for post-processing. To guarantee an accurate tracking of the tip leakage flow, a radial extension covering the outer 12.5% of the span has also been considered.

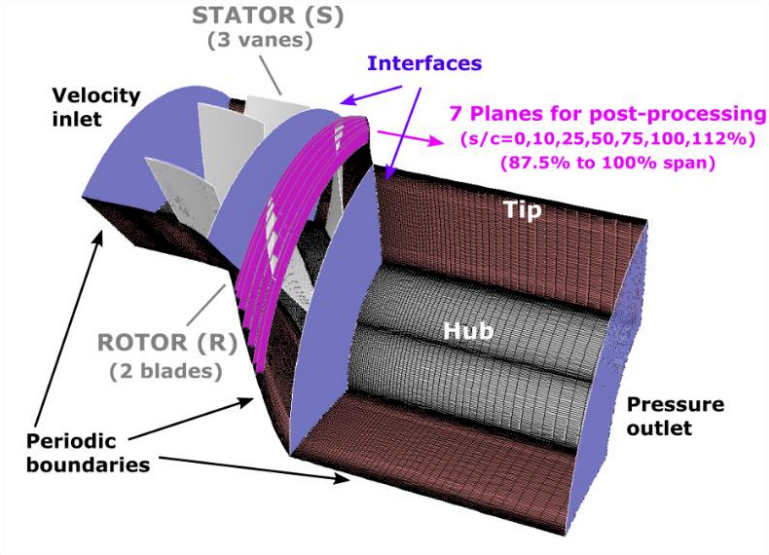

Figure 3. Three-dimensional view of the numerical domain.

3.2. Computational setup: meshing and BCs

Because of the large reduction in the number of vanes/blades to be modelled (from 22 to only 5), the spatial discretization of the internal passages of the axial fan can be extraordinary enhanced introducing high-dense meshes at affordable computational costs. This allows the modelling of the tip clearance by means of an unsteady simulation with reasonable CPU times.

A non-conformal mesh has been employed due to the different pitchwise lengths in both stator and rotor zones. A hybrid meshing strategy, introducing both structured and non-structured elements, was employed for an efficient meshing of the geometry. The following tables summarize some relevant indicators concerning the grid quality. Firstly, table 2 provides the averaged values of the equiangle skewness and the orthogonal quality of the grid cells in the different domains of the mesh. Secondly, table 3 also includes the equiangle skewness and the aspect ratio for the worst elements of the different cell types used in this hybrid mesh. The global equiangle skewness is very low (0.1), with a significantly high orthogonality (0.94) for the whole model. In addition, the worst skewness is always below 0.9 (as usually recommended in the literature) for the different mesh types, and the aspect ratio is large only in case of quadrilateral and triangular prisms in the midspan region (accommodated to the negligible radial velocities in those locations).

Table 2. Grid quality parameters for the different domains of the mesh.

Zone	Nº elements	%	Averaged cell equiangle skewness	Averaged orthogonal quality
Inlet (upstream)	189012	4.5	0.021	0.958
Stator	1777856	41.1	0.097	0.980
Rotor	1894026	43.8	0.258	0.773
Outlet (downstream)	459940	10.6	0.036	0.997
Total	**4320834**	**100.0**	**0.1**	**0.945**

Table 3. Grid quality parameters for the different cell types.

Type	Nº elements	%	Zones	Max. equiangle Skewness	Max. aspect ratio
Hexahedron	2979880	69.0	Inlet, Outlet, Stator & Rotor BL	0.879	182.2
Triangular prism	736472	17.0	Rotor Passage at hub (0-30% span) and tip (70-100% span)	0.845	4.63
Tetrahedron	590242	13.7	Rotor Passage (30-70% span)	0.724	5.81
Pyramid	14240	0.3	Rotor Passage (30-70% span)	0.869	35.2

In the tip region, fully structured blocks were piled up against the casing for an optimal gridding gap. A 15-cells discretization was finally clustered towards the endwall, leading to a typical $\Delta z^+ \sim 30$. Both vanes and blades walls were meshed using O-type grids with [100x25x80] elements in the stream, pitch and spanwise directions respectively, in order to maintain a y+ value below 11.225 and avoid the buffer layer for the enhanced wall treatment. In particular, averaged Δy^+ values ranged between 5.3 and 9.1 for both PS and SS of vanes for all the test conditions, while blades' PS and SS were kept between typical values in the range of 9.4 and 12.6. The number of cells in every rotor passage reached up to 0.9M cells while the number of points in the stator passages was around 0.7M cells, thus resulting in 4.3M cells for the whole domain. Note that the mesh density in that internal zones was carefully selected to capture vortical structures in the range of the integral length scales when large flow separations may take place (at near-stall conditions). Precisely, previous experimental investigations of the authors have determined that typical mesh sizes around 2 mm are required downstream of the rotor to describe those largest eddies (Fernández Oro *et al.*, 2007) This value has been further reduced to 0.5 mm close to tip and hub endwalls. Figure 4 shows the mesh employed on a rotor blade, detailing the tip clearance mesh.

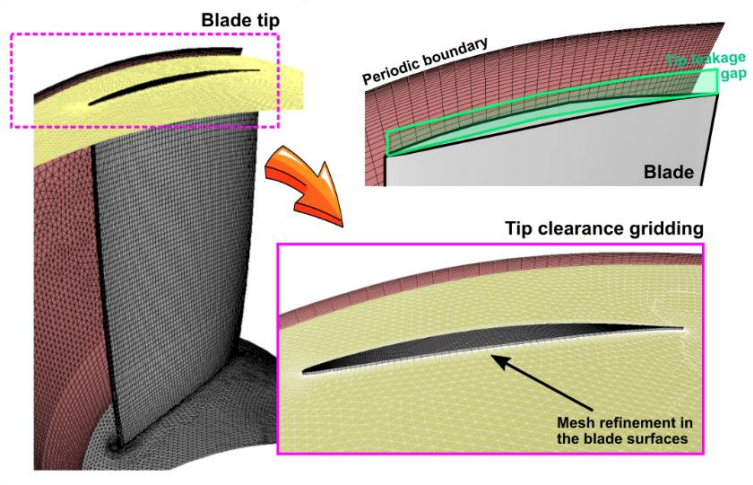

Figure 4. Rotor blade mesh. Detail of the grid refinement on the blade walls and in the tip clearance.

With respect to the boundary conditions, a set of periodic boundaries with an 80-deg tangential repeatability was introduced in both stator and rotor zones. At the inlet, a velocity profile (measured experimentally) was set as a prescribed incoming flow condition. Also, a radial distribution of the inlet turbulence levels was implemented according to measured data (levels in the range of 9% at the tip for a turbulent length scale of 0.13 m). Note that these conditions have been modified according to the volumetric flow rate to be simulated. At the pressure-outlet, a radial equilibrium condition was imposed assuming atmospheric gauge pressure. The solid walls are modelled as no-slip contours, stationary with respect to the adjacent cells. Therefore, to avoid the inclusion of additional interfaces in the tip clearance, the shroud velocity is set to zero referenced to the absolute frame. Though the cells in the gap are rotating embedded in the moving mesh of the rotor, the outer casing is modelled as a stationary wall.

3.3. Turbulence modelling

In eq. (2), the Reynolds Stress Tensor in the momentum equation has been modelled using an Eddy Viscosity Model, according to:

$$\tau_{ij} = -\rho\overline{u_i' u_j'} = \mu_t \underbrace{\left(\frac{\partial \bar{u}_i}{\partial x_j} + \frac{\partial \bar{u}_j}{\partial x_i}\right)}_{S_{ij}} - \frac{2}{3}\rho k \delta_{ij} \qquad (3)$$

being $k = \frac{1}{2}\rho\overline{u_k' u_k'}$, the turbulent kinetic energy and $\mu_t = \rho C_\mu \frac{k^2}{\varepsilon}$, the turbulent viscosity, with $C_\mu = 0.0845$. Moreover, the turbulence closure has been considered using a two-equation k-epsilon RNG turbulence model, because of its better agreement with experimental data for the present database than other one- or two-equation models commonly used in turbomachine flow simulations (see comparison in figure 5

below). In the case of the RNG model, these closure equations are for this case (neglecting buoyancy):

$$\rho\frac{\partial k}{\partial t}+\rho\frac{\partial(k\bar{u}_i)}{\partial x_i}=\frac{\partial}{\partial x_j}\left[\alpha_k\mu_t\frac{\partial k}{\partial x_j}\right]+2\mu_t S_{ij}S_{ij}-\rho\varepsilon \quad (4)$$

$$\rho\frac{\partial \varepsilon}{\partial t}+\rho\frac{\partial(\varepsilon\bar{u}_i)}{\partial x_i}=\frac{\partial}{\partial x_j}\left[\alpha_\varepsilon\mu_t\frac{\partial \varepsilon}{\partial x_j}\right]+C_{\varepsilon 1}\frac{\varepsilon}{k}\left(2\mu_t S_{ij}S_{ij}\right)-\rho C_{\varepsilon 2}\frac{\varepsilon^2}{k} \quad (5)$$

where the turbulent dissipation rate is defined as $\varepsilon=2\nu\overline{s'_{ij}s'_{ij}}$, being $s'_{ij}=\frac{1}{2}\left(\frac{\partial u'_i}{\partial x_j}+\frac{\partial u'_j}{\partial x_i}\right)$; and typical coefficients $C_{\varepsilon 1}=1.42$, $C_{\varepsilon 2}=1.68$ and $\alpha_k=\alpha_\varepsilon\sim 1.383$ have been employed.

Preliminary tests were also performed using S-A and SST k-ω turbulence modelling, as well as the RNG k-ε option. The radial distribution of the mean axial velocity downstream of the rotor was obtained for the different models and compared to the experimental values measured in the outer half of the passage. It must be noticed that due to constructive restrictions, the final assembly of the fan introduced a wide, unsealed cavity at the hub which was responsible for an excessive broadening of the inner casing boundary layer, as shown in the experimental measurements (Fernández Oro at al., 2007a; 2007b). Since this effect was not considered in the numerical modelling, only the comparison of the results in the outer half of the blade span are finally shown in the figure. It is also important to note that the tip flow structures are considered to be unaffected by those secondary flows at the hub because the bulk flow in the midspan region was found to be quite planar with negligible radial velocities. Figure 5 shows the results obtained for the three flow rate conditions analyzed. For nominal and partial load conditions, all the models exhibited a similar behavior. However, the k-epsilon version demonstrated higher accuracy at 70% of the nominal flow rate, thus being selected for the final set of simulations.

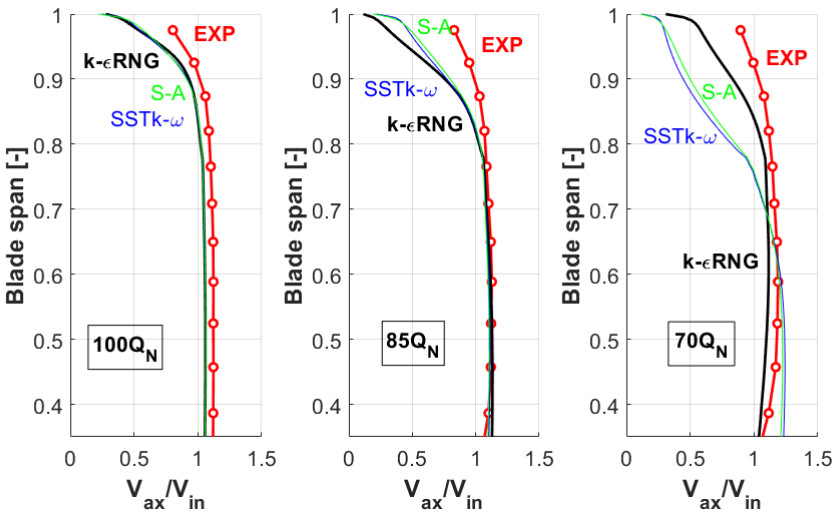

Figure 5. Comparison of different turbulence models for the preliminary tests.

3.4. Solution procedure and numerical convergence.

For the final set of simulations, a gradual procedure was executed to ensure stable convergence, following the guidelines proposed by Uzol *et al.* (2007). Basically, a steady solution using first-order schemes is initially resolved to be progressively updated using high-order discretizations in both turbulent transport and flow governing equations. The final step executes a full unsteady simulation that is extended up to 20 blade passing periods (i.e., as two complete rotor turns) so a well-established flow within the stages is attained. The numerical scheme was already described in section 3.1.

For an accurate selection of the time step, it was necessary to estimate the turn-out time of the largest eddies to be resolved. In the interrow region, a characteristic length scale in the order of L_{tip} ~ 6-8 mm was found in the tip region, with typical level of fluctuations as high as 25% (due to the casing BL, Fernández Oro *et al.*, 2007; 2019). For RANS computations, a rough estimation of the required time step size can be given if the time period of the expected fluctuations for the TLF are discretized within 10 to 20 time steps (as suggested in "Transient Calculations" - ANSYS Fluent Tutorial, Release 14.5, 2012). This leads to: $\Delta t_{RANS} \sim \frac{1}{15} t_{eddy} = \frac{1}{15} \frac{L_{tip}}{U} \sim 3 \cdot 10^{-5} s$, where U represents the velocity fluctuation of the relative flow in the blades. For convenience, a time step of $4.6296 \cdot 10^{-5}$ s was finally adopted since it is within the order of magnitude and it also describes one blade passing period with 60 time steps in the absolute frame. This implies a tangential angular displacement of 0.666 deg per time step (assuring a good description of the unsteady flows in turbomachinery environments according to the literature) and an exact multiplicity for the relative frame of reference (a blade faces a moving vane in the relative frame after 40 time steps). Nevertheless, in order to analyze the sensitivity of the time-dependent results in the CFD modelling with respect to the selection of the time step size, additional simulations have determined that the selected temporal discretization is sufficient to capture the instabilities associated with the interaction of the stator flow with the TLF. In particular, a reduced time step (for 120 time steps per blade event) has not shown a remarkable improvement in the results, while a larger time step (for 30 time steps per blade event) has revealed its inability to reproduce those interaction instabilities.

Approximately, 150 hours (1 week) of CPU time was necessary to resolve every case analyzed with the established convergence procedure. All the data set was executed on a home-made cluster consisting of four parallelized quad-core PCs at 2.67 GHz with 4 GB of RAM in each node. A convergence criterion of 10^{-5} was fixed for all the governing equations, which represented at least 50 iterations for each time step. A final execution of the model was always carried out during an additional blade passing to store all the flow variables in the planes of interest for the following post-processing.

3.5. Validation

Finally, a comparison between numerical and experimental results in the zones of interest are shown to validate the numerical methodology. In a global basis, the

performance curve is firstly calculated (Figure 6, top) to compare the numerical predictions with the available experimental data. The plot shows the total-to-total pressure coefficient, defined as $\psi = \frac{2\,\Delta p_T}{\rho U_{tip}^2}$, as a function of the flow coefficient, $\phi = \frac{V_{ax}}{U_{tip}}$. The grey line with circular markers corresponds to the experimental curve, while solid black squares represent the numerical estimations. Since the numerical model has simulated just the interior passages of the fan, it was necessary to perform a correction in the pressure outlet of the numerical model to take into account the expansion of the discharged flow. In particular, the corrected total pressure rise of the fan has been estimated according to this expression: $\Delta P_{fan,\ corr}^{t-t} = \frac{1}{2}\rho v_\infty^2 - P_{T,in}$, where v_∞ corresponds to the upstream velocity in the circular (not annular) inlet section of the fan; and $P_{T,in}$ represents the value of total pressure at the annular section of the rotor intet. Table 4 also shows the numerical values obtained for the cases simulated.

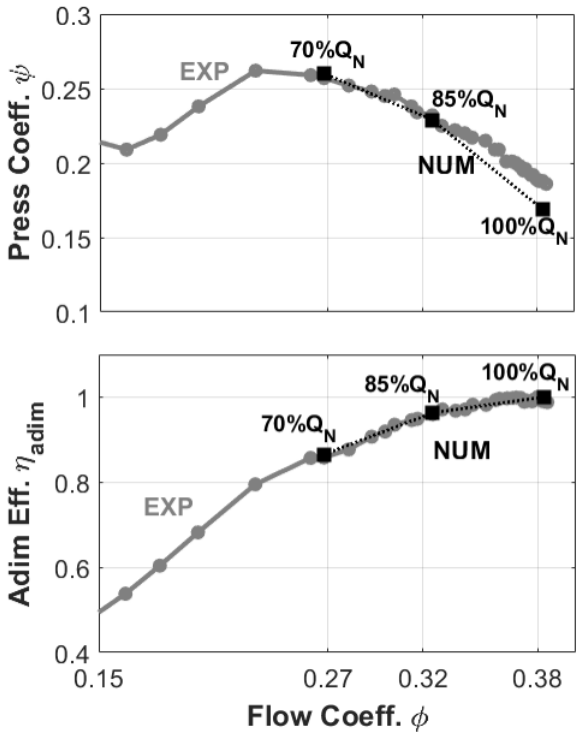

Figure 6. Fan performance curves. Comparison of experimental and numerical results.

Table 4. Numerical parameters and results from the simulations.

Case	Q (m^3/s)	ϕ [–]	ψ [–]	V_{in} (m/s)	$P_{T,in}$ (Pa)	$\Delta P_{fan,corr}$ (Pa)
100% Q_N	16.5	0.383	0.170	39.5	-497	**1083.5**
85% Q_N	14.0	0.325	0.229	33.5	-1042	**1464.3**
70% Q_N	11.5	0.268	0.259	27.6	-1369	**1653.4**

Figure 6, bottom, also shows the comparison of global efficiencies for both numerical and experimental results. Since the experimental data provided an overall efficiency including mechanical and electrical losses of the driving motor, the plot has been made non-dimensional (using the maximum efficiency at nominal conditions) to obtain a

global trend valid for compassion with the CFD data. The numerical efficiency has been computed according to $\eta = (\Delta P_{fan}^{t-t} \cdot Q)/(M_{blade}\omega)$, considering the pressure rise directly from the computations without using the pressure correction (otherwise, the torque on the blades should have been corrected as well). Despite these restrictions, the estimations obtained for off-design conditions are remarkable.

In addition to this accurate global comparison, validation of more detailed flow variables is also mandatory. Previous figure 5 showed a reasonable agreement between the numerical and experimental distributions of the axial velocity rotor downstream. However, for a major insight, the ensemble-averaged values of the instantaneous static pressure measured in the fan casing have been compared with the experimental computations. For that purpose, a pressure coefficient for the signal fluctuations obtained with the transducers has been defined according to $C_p = \frac{p-\bar{p}}{0.5\,\rho V_{in}^2}$, where the overbar denotes the overall, mean-time static pressure, computed as the time-averaged value of the unsteady pressure fluctuation. Figure 7 has been included to show the comparison in the absolute frame of reference for all the conditions simulated. The left contours illustrate the experimental fluctuations observed for a complete stator pitch (in the x-axis and triplicated for readability) during a blade event (in the y-axis and duplicated). The results were measured at the midchord of the blades in the tip shroud. The transversal blue bands represent the lowest pressure levels corresponding to the core of the tip vortex (labelled as TLF trajectory in violet). Note that the inclination of those bands is a consequence of the tangential motion of the rotor flow structures in the absolute frame. Conversely, the diffused transversal band showing higher levels corresponds with the high-pressure region of the blades pressure side. A slight discontinuity at $t/T_B=1$ is observed for the time duplication, being more evident for the off-design conditions (85% and 70% Q_N). This is a consequence of the major disorder of the flow that leads to a lack of full periodicity associated with the occurrence of flow instabilities. Although the low-pass filter used for the signal preconditioning of the measurements has removed part of the instabilities, it still preserves significant amount of turbulent energy in the background (note the all-range scales embedded in the contours). Note also how the regions with minimum pressure coefficient (blue transversal bands) are progressively slimming as the operating flow rate is reduced. Moreover, for these experimental results, the periodic effect of the vanes is masked by the rotor gradients, at least for the evolution of the static pressure measured in the shroud with the available transducers.

On the right side of the figure, the numerical results have been represented using the same convention and color scale to ease the comparison. As expected, lower levels of residual instabilities are observed but the main structures associated to the tip vortex motion are well-reproduced. The lack of perfect temporal periodicity indicates again the level of flow disorder inherent to near-stall conditions. In the case of 100% and 85% Q_N, the impact of the stator flow structures on the TLF of the rotor is predicted by the CFD simulation, revealed as slight modulations in the intensity of the TLF (see vertical, white dashed lines in the maps). These representations also advance a lateral displacement

(towards the inner regions of the passage) in the trajectory of the tip vortex core in the case of nominal conditions with respect to the partial-load working point (see the inclined, violet dashed lines tracking the displacement of the vortex core). This observation is confirmed later in Figures 14 and 15.

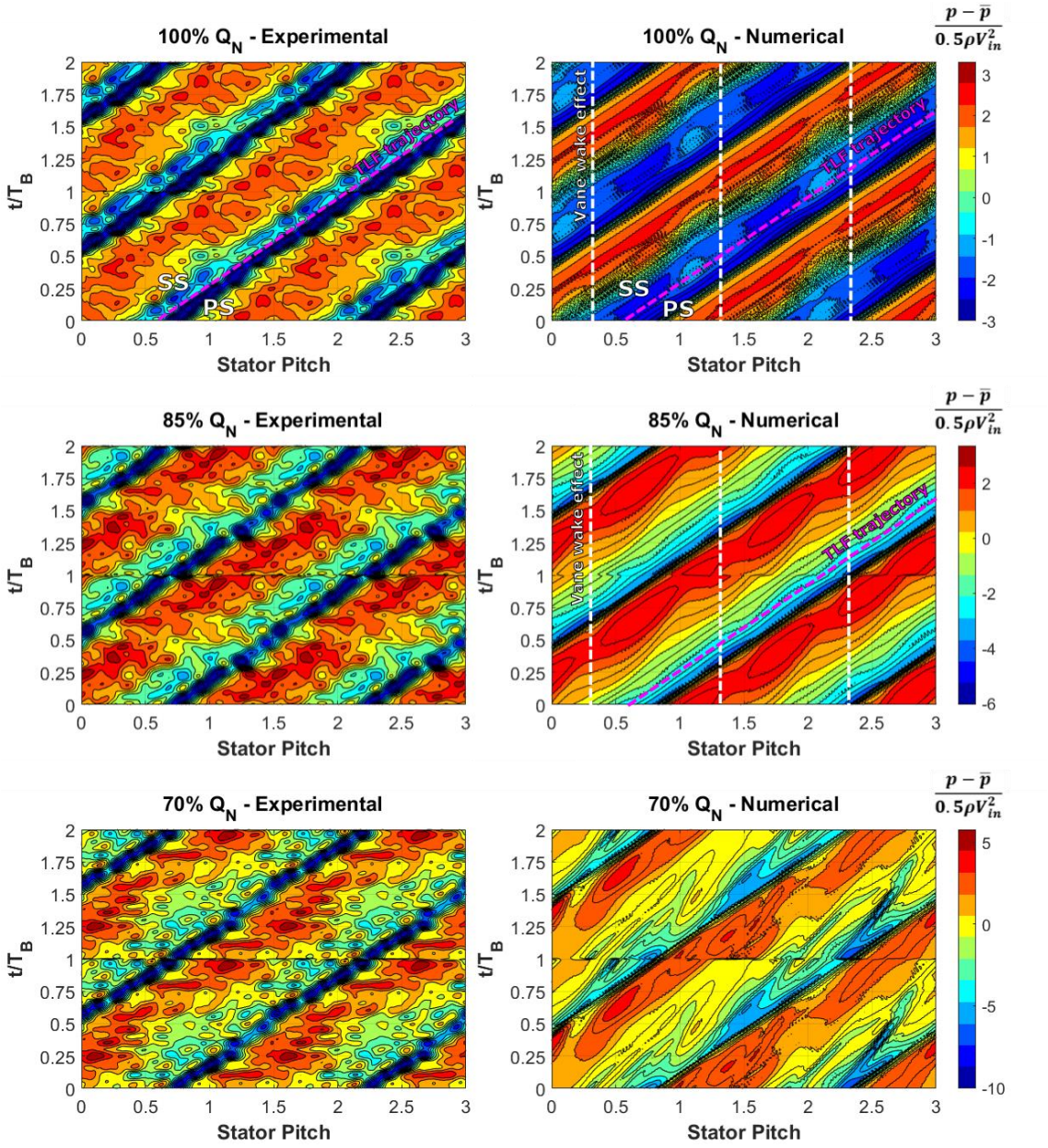

Figure 7. Pressure fluctuations in the casing. Experimental and numerical results.

To see more clearly how the tip leakage flow (attached to the rotor frame) is modified by the passing vanes, it is more convenient to see the results in the relative frame of reference. Therefore, these results have been also transformed into the relative frame and then time-averaged to show the blade-to-blade pressure distribution in the rotor tip at midchord. Removing the unsteady part, the impact of the vanes' non-uniformities vanishes and only the mean distribution of the pressure gradients along the rotor pitch in the tip region is preserved. More details about the

mathematical routine can be found in Fernández Oro et al (2008). Figure 8 compares these distributions for all the flow rates studied in both experimental and numerical data. The grey lines represent the experimental distributions while the black lines provide the numerical results. For all the cases, a reasonable prediction is observed considering the level of approach provided by the URANS computations. The maximum range of fluctuations is well predicted in the modelling (i.e., the peak-to-peak amplitude of the pressure fluctuations), with the minimum value progressively decaying as the flow rate is reduced (roughly -3, -4 and -6 for 100%, 85% and 70% flowrates respectively). Although the experimental distributions exhibit more ripples in the suction side than the numerical results, the time-resolved description of the pressure gradients in the tips is reasonably well-computed, with accurate extreme values and fluctuating rates. The maximum discrepancies are observed at nominal operation of the fan, where the CFD results predict a more intense pressure drop developed from the mid-passage to the suction side of the adjacent blade. Later, figure 9 will show how this deficit is associated to the path of the tip vortex, rolling up with its maximum strength at that location, although experimental data does not really confirm this pattern. Hence, it advances a presumably correct computation of the tip flow driven by those pressure gradients and encourages for further analysis of the present numerical database.

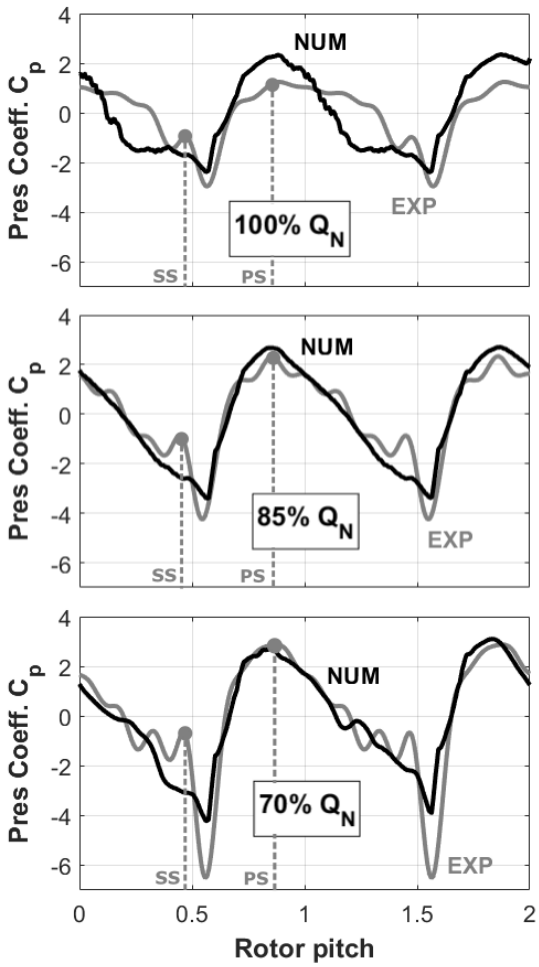

Figure 8. Mean-time distributions of the pressure fluctuations in the relative frame of reference at the fan casing. Comparison of experimental and numerical results.

4. RESULTS AND DISCUSSION

A detailed analysis of the leakage flow computations in the inlet vaned axial fan operating for three different working conditions is discussed below. The main objective is to quantify the impact of the deterministic turbulent scales of the upstream vanes over the unsteady evolution of the leakage flow in the rotor passages.

4.1. Tip Leakage Vortex (TLV)

Firstly, the evolution of the TLV along the blade passage is observed in the seven post-processing planes defined for the analysis. A typical metric, the total pressure loss coefficient (ξ_L) has been adopted to observe the differences in strength and features of the tip vortex according to flow rates. This coefficient is defined as the difference between the local and inlet total pressure divided by the inlet dynamic pressure. Figure 9 shows the mean-time description of the tip vortex trajectory in the relative frame of the rotor. A low velocity region, associated to the tip vortex is progressively mixed out along the blade passage, in consonance with previous results in the literature (Basson and Lakshminarayana, 1995; Bae *et al.*, 2005). Also, the values found here (up to -5) are coherent with previous levels reported in other studies. The leakage flow rolls-up into an incipient tip vortex between s/c=0.25 and 0.5 presenting there its maximum strength. At higher s/c, the vortex is convected from the suction side of the blade towards the center of the passage, and successively, interacts with the pressure side of the blade just before exiting the blade passage. The residual vortex is no longer shifted in the circumferential direction avoiding the arising of a double leakage flow (Tan, 2005). In other words, the trajectory of the tip vortex is not sufficiently tangentially inclined to climb over the adjacent blade and initiate a double leakage flow.

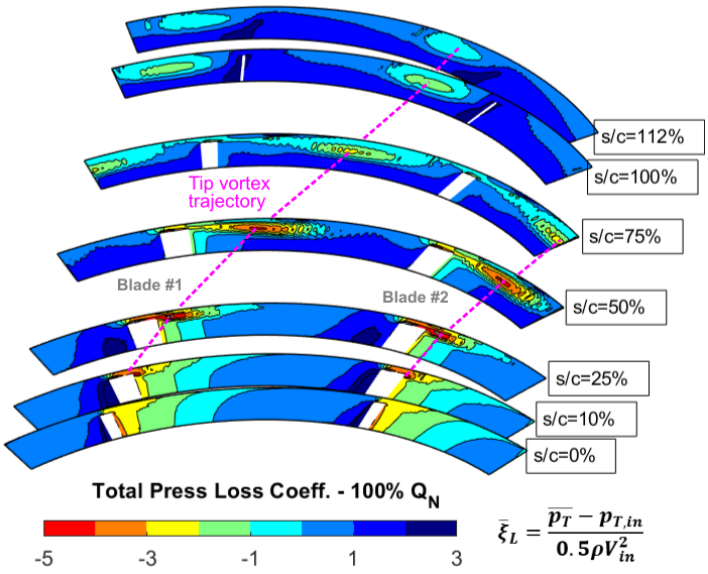

Figure 9. Spatial evolution of the tip vortex in the tip region at nominal conditions.

The structure of the mean-time vortex is presented in figure 10 in the case of partial load conditions. The prevalence of the TLV is masked towards the endwall casing as a consequence of a major flow disorder. In particular, the locus of the tip vortex is identifiable only until midchord, which is rapidly diffused due to the significant generation of losses close to the blade trailing edge. The maximum strength is now developed in the planes between s/c=0.1 and 0.25 as a consequence of the axial displacement of the stagnation conditions and the aerodynamic load towards the blade leading edge. The minimum value reached by the vortex core (around -6) also indicates the higher strength of the vortex at off-design conditions. Note also how the impact of the tip leakage flow in the flow conditions of the passage is significantly reduced.

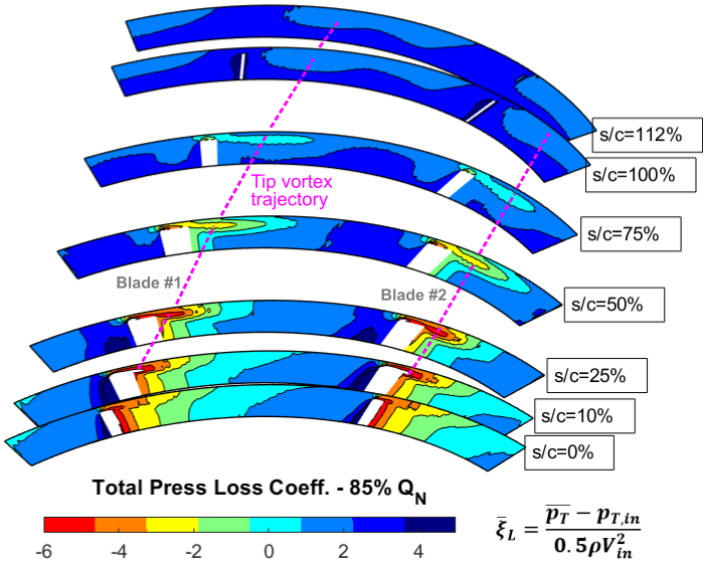

Figure 10. Spatial evolution of the tip vortex in the tip region at partial load conditions.

For the results of near-stall conditions (showed in Figure 11), the scale has been notably enlarged, especially towards the positive values, thus clearly indicating that stagnation conditions are severely reinforced; i.e, the relative flow is excessively overturned at the rotor inlet, so the flow impinges the blades' leading edge with an excessive incident angle increasing the pressure load and the generation of losses. Precisely, the pressure losses associated to the suction side of the blades are also increased, pointing out the presence of massive flow separations that are practically developed for the whole pitch of the blade passage. In this case, the tip vortex has no relevance in the tip region: instead of a trajectory with a low coefficient core (typical of the vortical pattern), the evolution of severe losses linked to the convection of the stagnation blockage is now the predominant mechanism in the tip region.

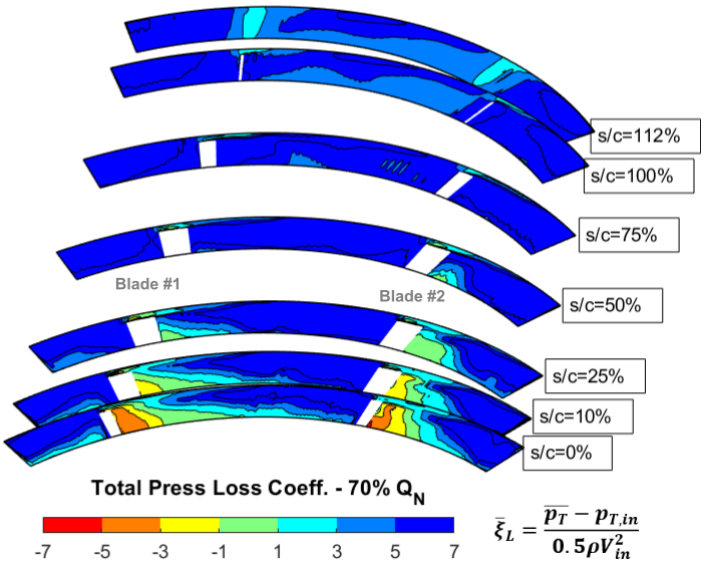

Figure 11. Spatial evolution of the tip vortex in the tip region at near-stall conditions.

An additional discussion is now given concerning the fluctuations observed in the TLV due to the periodic impact of the stator wakes. For that purpose, the RMS value of the loss coefficient is represented in Figure 12 to illustrate those regions with high levels of fluctuations in the tip vortex structures. These values account for the averaged value of the pressure fluctuations, so they are evaluating the location and instabilities of the shear layers associated with the vortical structures. Note that high values are found in the lateral shear layers of the tip vortex trajectory, thus revealing that the instabilities due to the impinging of the stator wakes are primarily manifested there. This is because the stator wakes at the tip are weakened as they are convected along the rotor passage (partially mixed-out with the casing boundary layers). Consequently, they do not have enough momentum deficit to modify the core of the leakage flow, and only the external zones of the vortex shear layers are influenced by that wake transport. Then, the interaction of the TLF with the vane wakes is perceived as periodic instabilities in that shear layers. The major interaction is observed at s/c=50%, though these averaged values should be compared to the local levels of the loss coefficient. This is further discussed in following figure 15, left plot (see the maximum peak of the RMS value at 100% Q_N).

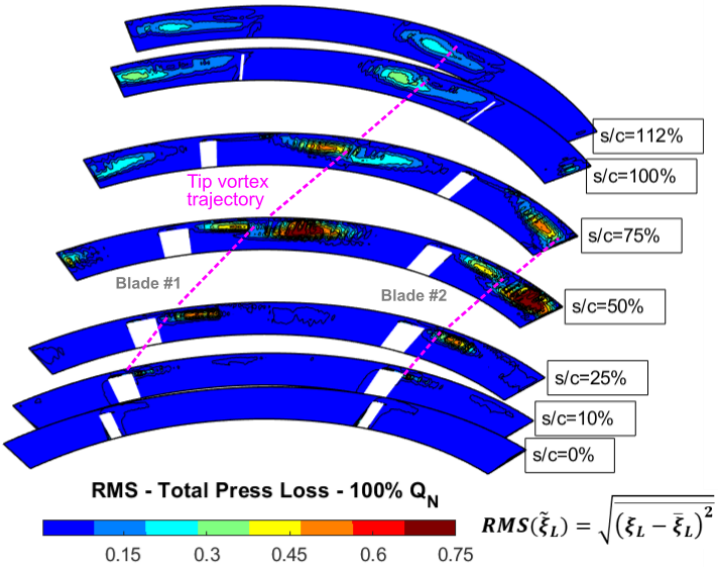

Figure 12. Instabilities of the tip vortex in the tip region at nominal conditions.

In the case of partial-load conditions (figure 13), the major fluctuations are derived from the separated flow regions at the suction side, which evolve along the blade passage towards the pressure side of the adjacent blade. Tip leakage flow forces the low-velocity regions associated to the detached conditions to move towards the inner locations of the passage. These are now the instabilities that are expected be modulated by the periodic passing of the impinging stator wakes. Because the tip vortex trajectory was not revealed for the mean-time distribution of the loss coefficient at near-stall conditions, maps of instabilities in the tip region are not shown for the 70% Q_N case.

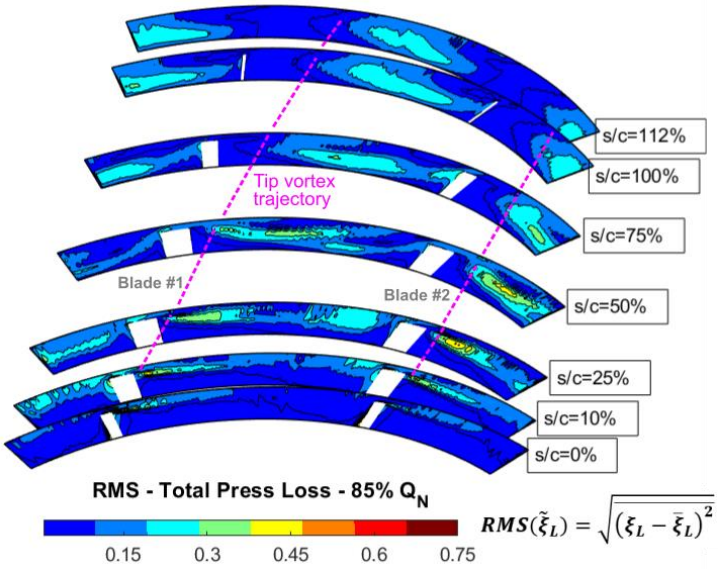

Figure 13. Instabilities of the tip vortex in the tip region at partial load conditions.

The quantification of the inherent instabilities associated with the vortex structures in case of a rotor-only fan is also an interesting question. For that purpose, additional simulations were performed suppressing the stator vanes (but with an inlet, circumferentially-averaged prerrotation) for a reduced model. In the case of the rotor-only model, no significant instabilities are observed in the streamwise evolution of the TLF (Figure 14, right). On the contrary, the stator flow interacts clearly with the vortex, meandering its trajectory and chopping the tip leakage flow downstream (Figure 14, left). The figure also shows how the high-velocity jet in the TLF moves tangentially towards the TE of the adjacent blade in the rotor only model (right map), while the unmixed stator-wakes prevent such rapid diffusion with a less tangential trajectory in the stator-rotor model (left map). At off-design conditions, the major level of disorder of the flow (as discussed earlier) masks all these effects, neglecting remarkable interactions with the stator flow.

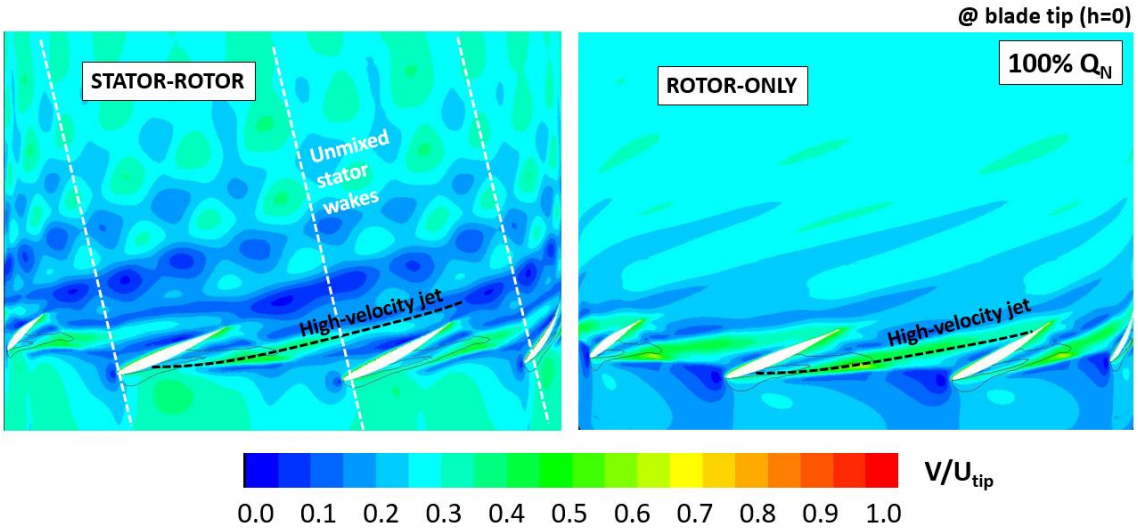

Figure 14. Comparison of TLF results for nominal conditions between the full stator-rotor model (interaction) and the rotor-only model (no interaction)

To conclude this section, the trajectory of the tip vortex and the intensity of the instabilities (in percentage, comparing the RMS value of the loss coefficient with its local value in the vortex) is provided in Figure 15 for both 100% (black thick line) and 85% Q_N (thin line) flow conditions. The results for the rotor-only case at nominal conditions are also given for comparison (grey line). The left plot tracks the vortex trajectory along the chordwise direction (y-axis), revealing the tangential displacement of the vortex (x-axis). Note the evident differences in the circumferential motion of the vortex as a function of the flow rate, mainly conditioned by the separated flow in the suction side of the blades at partial flow rate. In the right plot, the mean fluctuation (in percentage) provides a good metric of the influence of the stator wakes in the TLV. At nominal conditions, the maximum impact is quantified in a 18% at the midchord, though typical values around a 10% are observed along the whole chord. For off-design conditions, this impact is significantly reduced, reaching up to just a moderate 5%. In the case of the rotor-only model, the trajectory is clearly displaced towards the blade passage (as shown before in

Figure 14) with very low fluctuations associated with inherent instabilities of the vortex flow (no interactions).

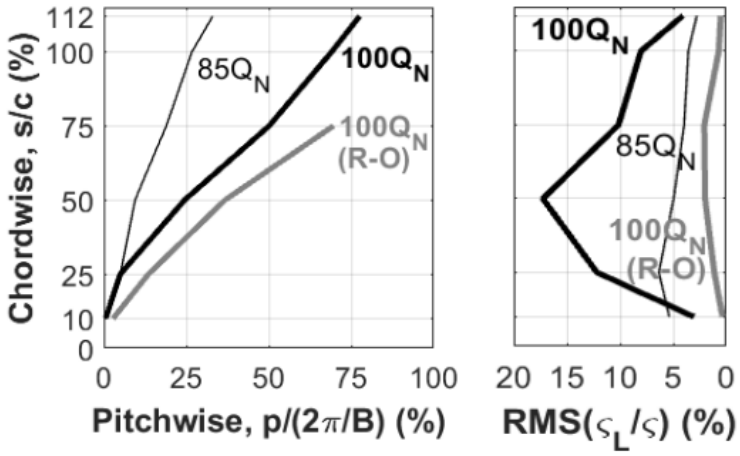

Figure 15. Trajectory of the tip vortex (left plot) and chordwise distributions of the tip vortex instabilities (right plot) for both nominal and off-design conditions (black lines). Comparison with results of a rotor-only model (grey lines).

4.2. Tip Leakage Flow (TLF)

4.2.1. Unsteady tip velocities

In this section, the leakage flow established in the tip clearance of the blades is analyzed. The data obtained in the seven transversal planes for the post-processing is used to compute the unsteady tip velocity perpendicular to the gap, according to: $V_{TL} = V_{tg}cos\theta - V_{ax}sin\theta$, where θ represents the stagger angle of the blades at the tip region (see table 1). The kinematic considerations followed are shown in figure 16.

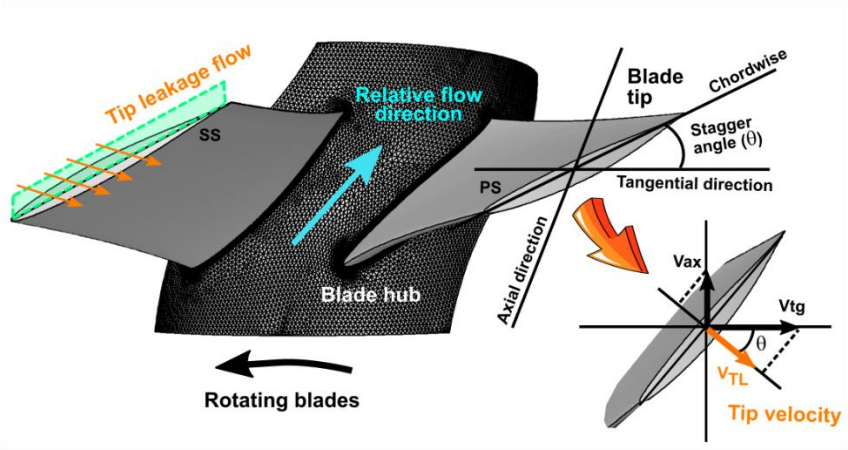

Figure 16. Kinematic considerations to compute the tip leakage velocity.

A first look at the impact of deterministic sources on the evolution of the tip flow is revealed in Figure 17 for the nominal case. The figure plots the temporal evolution of

the tip flow over one vane passing period through the mapping of eight intermediate snapshots. The tip velocity, VTL, has been normalized by the inlet axial velocity, according to the values shown in table 2. In correspondence with previous maps showing the generation of the TLV, maximum jets are found in the central sections of the blade, between s/c=0.4 and 0.5. The velocity intensity is found to be up to 1.5 times higher than the bulk velocity of the operating flow rate. As the stator wakes are impinging in the tip region, a significant modulation is observed in the maps, especially in the first half of the vane cycle (from t/T_V=0.00 to 0.50). With respect to the spanwise distribution, the velocity has a clear tendency to be radially displaced towards the endwall casing.

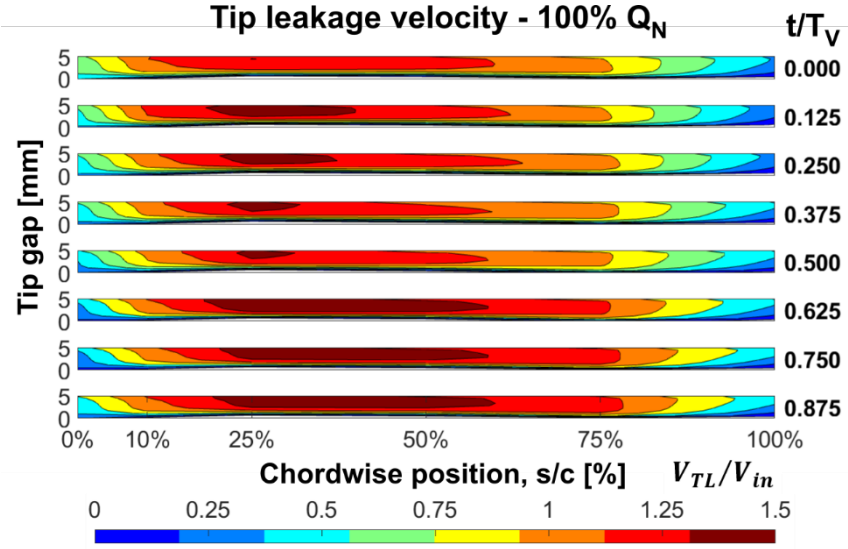

Figure 17. Unsteady distribution of the tip leakage velocity at nominal conditions.

In the case of an 85% of the nominal flow rate (figure 18), the regions with maximum tip velocities are significantly shifted towards the leading edge of the blades (at chord positions around s/c=0.1). In addition, its intensity is significantly enhanced, reaching up values as high as twice the mean through-flow velocity of the fan stage. The periodic impact of the vane flow structures is noticeable again with fluctuations in the extension of the large velocity regions. Close to the trailing edge, a small portion of reversed flow is found between s/c=0.85 and 1.0, indicating the presence of detached flow close to the tip wall of the blades.

Finally, figure 19 shows the results for the near stall condition. The temporal evolution of the tip velocity maps reveals the significant instabilities associated with this flow condition. As expected, the high velocity regions are reinforced with respect to previous cases, being as high as 2.5 times the bulk flow velocity. On the contrary, severe reverse flow is established in the vicinity of the trailing edge, established from s/c=0.8 to 1.0. The periodic impact of the vane flow structure is also remarkable, especially at t/T_V=0.5 and 0.625 where reverse flow is even triggered in the leading edge zone of the tip. This effect is a consequence of the convection of detached flow shed from the upstream vanes, which interacts with the casing boundary layer, rolling up, and finally impinging

of the tip gap. Due to this secondary vertical effect, the high velocity regions are partially shifted toward the blade tip wall in the radial direction.

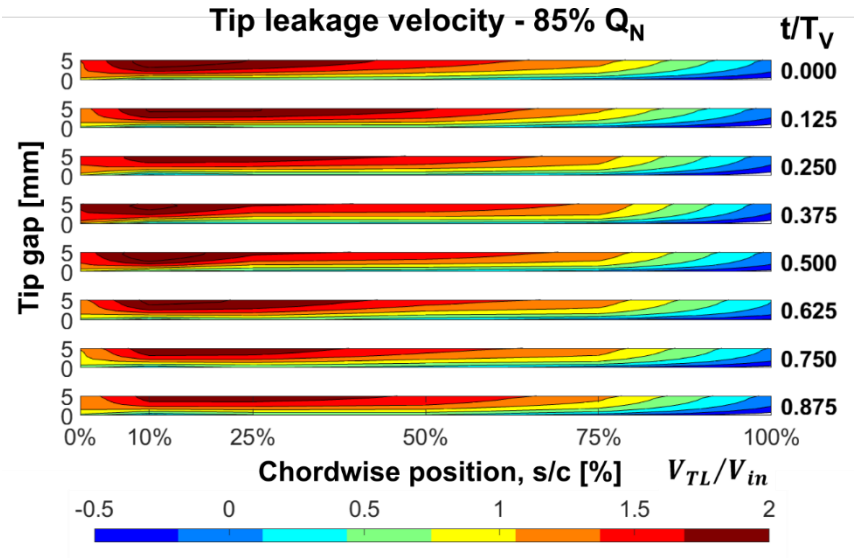

Figure 18. Unsteady distribution of the tip leakage velocity at partial load conditions.

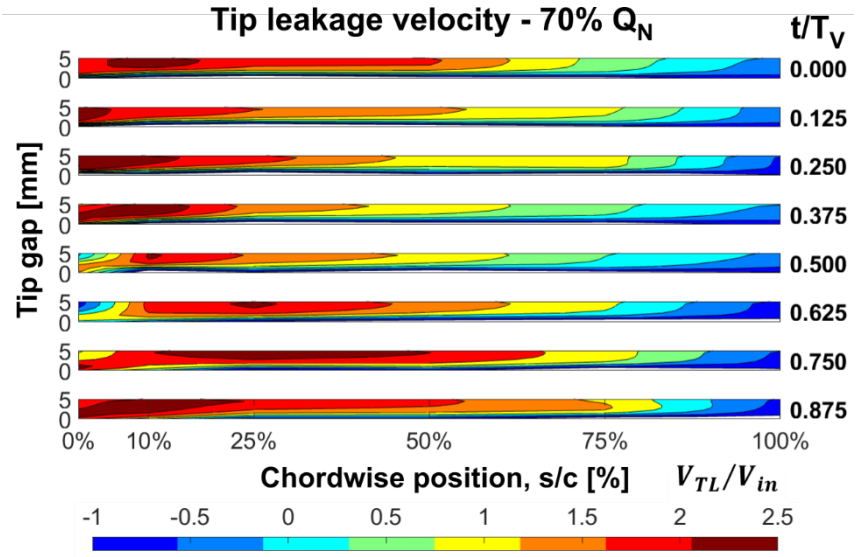

Figure 19. Unsteady distribution of the tip leakage velocity at near stall conditions.

The radial distribution of the tip velocity at midchord (s/c=0.5) has been extracted from figures 17 to 19 and compared with experimental estimations obtained from the measurements of the pressure transducers. Figure 20 presents in black lines the mean-time distribution obtained from the URANS computations for the three different flow rates analyzed. In addition, solid gray lines (up to forty in every plot) correspond to the radial distribution in every intermediate time step covering the whole vane passing period. Note that, at this chordwise position, the fluctuation of the velocity profiles

increases as the flow rate is progressively reduced, being particularly intense at 70% Q_N due to the interaction effects. It is also remarkable that stable reverse flow in the first millimeter of the gap (close to the blade) is clearly predicted by the CFD model, especially at off-design conditions. This suggests large detached regions of flow in the transversal direction with respect to the tip gap. Moreover, the pressure ranges measured experimentally at the pressure and suction side of the blades with the transducers (and shown in figure 8 with dashed lines) have been employed to estimate the velocity of the driven jet in the gap according to: $V_{TL}^{(\exp)} = C_D\sqrt{\frac{2(p_p - p_s)}{\rho}}$, as suggested by Storer and Cumptsy (1991). A typical discharge coefficient of C_D=0.6 for an abrupt expansion has been employed, with the pressure values summarized in table 5. The non-dimensional values obtained in the last column of the table have been included in the plots as a dashed red line for reference, showing a reasonable magnitude.

Table 5. Estimation of tip velocity at s/c=0.5 from experimental pressure measurements.

Case	Q (m^3/s)	P_p (Pa)	P_s (Pa)	$V_{TL}^{(exp)}$ (m/s)	$V_{TL}^{(exp)}/V_{in}$ (m/s)
100% Q_N	16.5	-900	1160	35.1	0.89
85% Q_N	14.0	-580	1567	35.9	1.07
70% Q_N	11.5	-300	1310	31.1	1.12

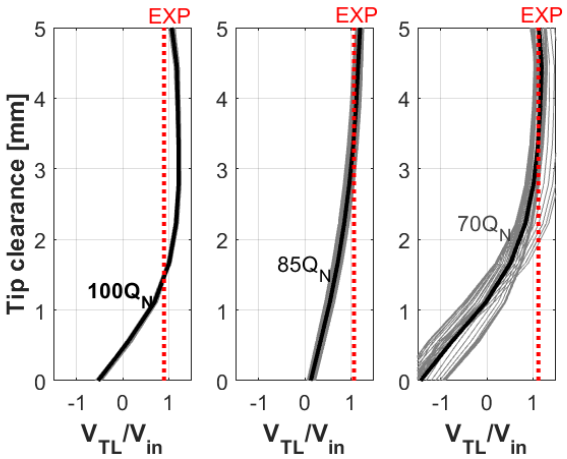

Figure 20. Radial distributions of the tip velocity at s/c=0.5 and comparison with experimental estimations from pressure measurements in the tip gap.

4.2.2. Computation of the tip leakage flow

Additional insight is made on the tip leakage flow representing, firstly, the mean-time distribution of the tip velocity along the chordwise position (see figure 21). These values have been obtained from the spanwise averaging of the numerical results in the tip gap. In this case, the tip leakage velocity is made non-dimensional by the blade velocity using a typical convention found in the bibliography. A characteristic U distribution is found for nominal conditions, with a plateau equal to V_{TL}/U_{tip}=0.33 in the major part of the

axial extension of the tip clearance. This value is similar to other studies in the bibliography analyzing axial machinery with corresponding flow coefficients and tip gaps (Miorini et al., 2012). As the flow rate is decreased, a progressive decay of the tip velocity (even towards reverse flow) is found in the second half of the blade chord (from s/c=0.25 on), being especially intense in the case of the 70%Q_N. Also, the experimental estimations measured at the midchord are introduced as a reference (solid dot, 100%Q_N; white dot, 85%Q_N; cross, 70%Q_N).

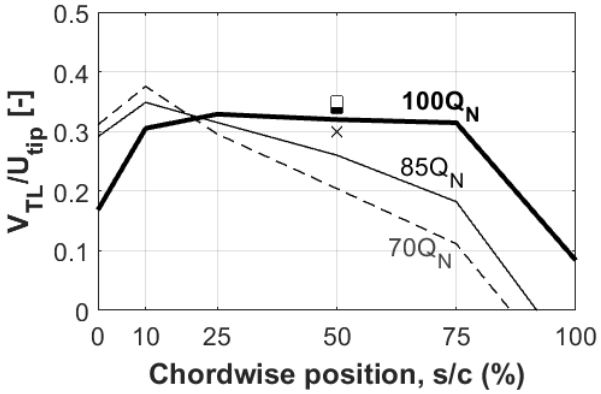

Figure 21. Chordwise distribution of the tip leakage velocity as a function of the flow rate.

Secondly, through the numerical integration of the tip leakage velocity in the tip gap, it is possible to obtain the time-resolved evolution of the tip leakage flow during one vane event in the relative frame. This is shown in figure 22 for the three flow rates analyzed and duplicated for convenience. Both nominal and partial load conditions exhibit a periodic response, thus indicating that the deterministic contributions associated with the stator interaction have an impact on the evaluation of the overall tip flow of a blade. In the case of near stall conditions, a major flow disorder which it is associated with severe flow separations in the stator vanes (but not-clocked with the periodic vane motion in the relative frame) is responsible for large oscillations as shown in the dashed grey line of the plot. Table 6 summarizes the mean-time values of this temporal evolutions. In particular, the mean tip leakage flow at nominal conditions in a single blade is 0.226 m^3/s, which represents a 12.4% of the total flow rate (referenced to one ninth of the upstream flow rate). At partial conditions, the leakage flow is slightly reduced to a 11.3% while at near-stall conditions an abrupt reduction to just a 6.7% is experienced due to the massive flow separations and the arising of large zones with reverse flow as shown previously. The table also quantifies the effect of the deterministic fluctuations on the time-resolved evolution of the leakage flow. Comparing the RMS value of the fluctuations observed in the plots (fifth column) with the mean-time values, it is concluded that both 100% and 85% Q_N conditions present a deterministic impact around 2.8 and 3.4% respectively (sixth column), while at 70% Q_N, non-deterministic contributions induce large fluctuations up to a 33.6% in average. Finally, the results of the rotor-only model reveal that the TLF is higher (from 12.4 to 14.5%) in the absence of inlet guide vanes, and with a very low level of oscillation.

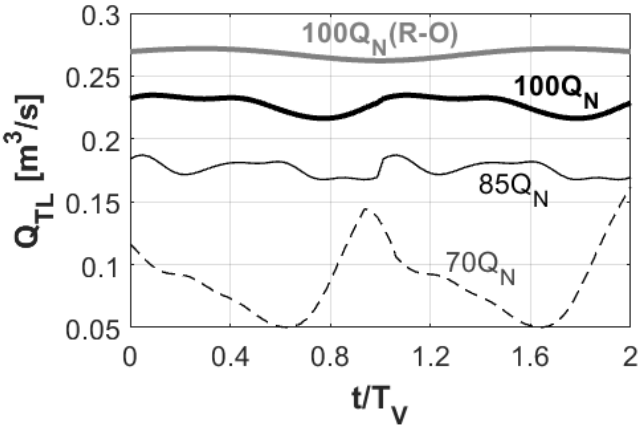

Figure 22. Time-resolved evolution of tip leakage flow as a function of the flow rate.

Table 6. Averaged values of the tip leakage flow as a function of the flow rate

Case	Q/N_b (m^3/s)	Q_{TL} (m^3/s)	Q_{TL}/Q [%]	RMS(Q_{TL}) (m^3/s)	RMS(Q_{TL})/ Q_{TL} [%]
100% Q_N	1.83	0.226	12.4	0.0064	2.85
85% Q_N	1.55	0.175	11.3	0.0061	3.45
70% Q_N	1.27	0.085	6.70	0.0291	33.6
100% Q_N (R-O)	1.85	0.268	14.5	0.0033	1.24

4.2.3. Turbulent and deterministic fluctuations

To conclude the analysis of the results, the turbulent structures of the flow, in terms of turbulent kinetic energy (TKE), are compared to the deterministic energy budget in the tip regions of the axial fan. As a starting point, the unsteady evolution of TKE, made non-dimensional with the square of the bulk velocity, is shown along the chordwise coordinate in the tip clearance (Figure 23). For convenience, the maps have been duplicated along the y-axis to show the periodicity of the distributions with the vane passing period (T_v). At nominal conditions (left map) the maximum generation of TKE is revealed at s/c=0.25 to 0.4, in accordance with the position of the maximum jet velocity in the tip. Maximum non-dimensional values reach up to 0.2 times the kinetic energy of the mean flow velocity. Moreover, the deterministic interaction of the vanes is also remarkable (repeating maximum values at t/T_V=0.25 and 1.25), thus concluding that the generation of turbulence, due to the high tip velocities in the gap, is also conditioned by deterministic contributors with fluctuations up to 25%. At both 85% and 70% Q_N, the progressive displacement of the regions with maximum TKE towards the blade's leading edge is confirmed. The periodicity is not so evident, especially at near-stall conditions, as pointed by the discontinuity in the map representations at t/T_v=1.0 all along the blade chord.

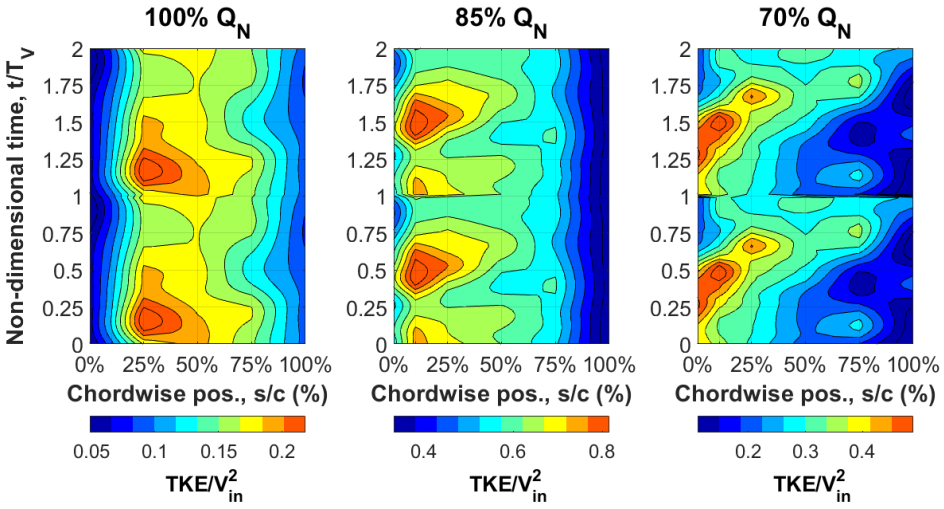

Figure 23. Unsteady evolution of TKE distributions in the tip gap along the chordwise position. Comparison of different working conditions.

Additionally, the Deterministic Kinetic Energy (DKE), computed as the mean-time contribution of the unsteady, periodic fluctuations of the flow in the tip region, has been represented in the tip clearance comprising the whole tip clearance along the blade chord in Figure 24. For all the flow rates, this component results significantly lower than the TKE, being specially concentrated towards the leading edge of the blades. At nominal conditions, maximum values are roughly one order of magnitude lower than turbulent scales, thus confirming that interaction effects have a moderate effect (in the tip leakage flow, it was quantified in a 3% approximately). At partial conditions, they are also reinforced but maintaining the same proportion with respect the TKE levels in the tip gap.

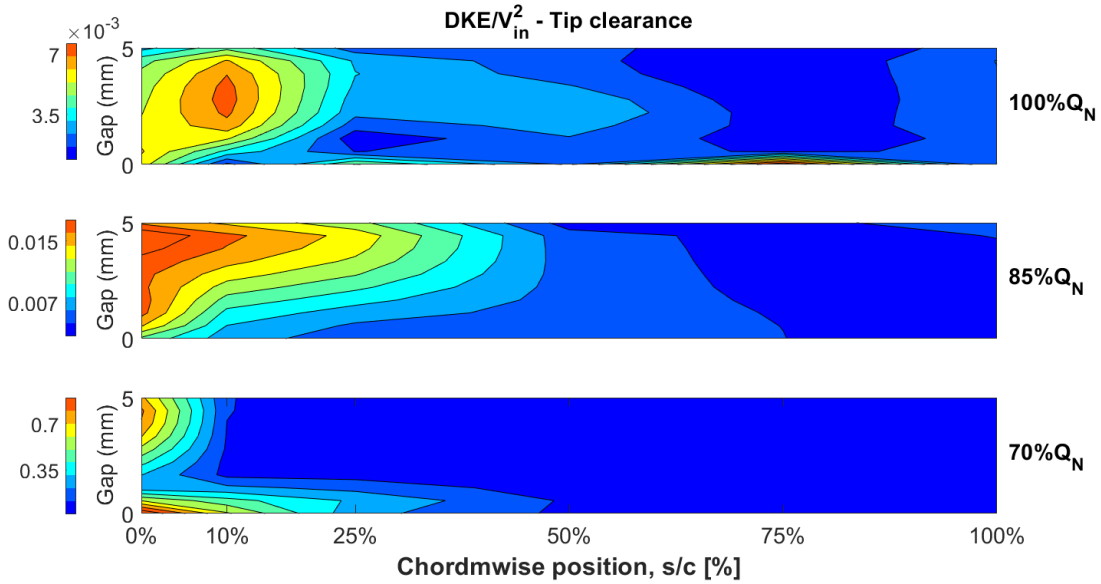

Figure 24. Distributions of Deterministic Kinetic Energy in the tip gap along the chordwise position. Comparison of different working conditions.

Finally, the mean-time distribution of the TKE maps are presented in figure 24, left, in order to show the typical ranges observed in the tip gap region for the different flow rates. On the right, the plot presents the corresponding distributions in the case of the DKE (spanwise-averaged). Because of the extremely high fluctuations observed in the leading edge at near-stall conditions, the deterministic energy is severely overproduced, mainly associated with unstable detached flow coming from the blades (non-periodic effect) that has been masked as deterministic unsteadiness in the averaging procedure. In the other cases, the reduced values of DKE have been represented in the lower subplot with a reduced scale, pointing out its moderate impact over the primary flow structures associated to the tip vortex formation. These values are consistent with the level of oscillation in the tip leakage flow reported in table 6, with typical values around 3% for stable working conditions.

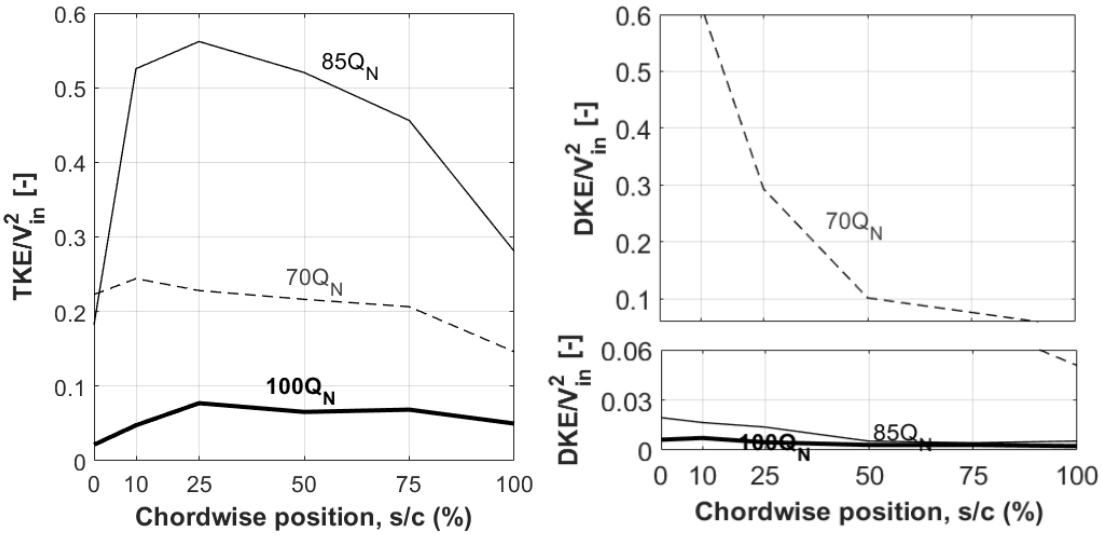

Figure 25. Comparison of chordwise distributions of TKE and DKE.

5. CONCLUSIONS

Experimental and numerical methodologies have been used to describe the influence of the stator-rotor interaction on the tip leakage flow of a single-stage low-speed axial fan. In particular, URANS modelling that resolves the three-dimensional, unsteady flow in the tip clearance of the blades has been used by implementing the sliding mesh technique. Different operating conditions have been studied, modifying the flow conditions, and the numerical model has been validated using experimental measurements taken with piezoelectric pressure transducers to characterize the unsteady pressure in the casing of the turbomachine.

The evolution of the tip vortex has been observed in the tip region of the rotor passages of the fan, addressing its characteristics as a function of the flow rate. The vortex is rolling up at different chordwise positions, depending on the operating flow rate, with a clear trend to shift towards the leading edge of the blades as the flow rate is reduced.

Its trajectory has been clearly identified for cases for nominal (100% Q_N) and partial load conditions (85% Q_N), while it is completely masked at near-stall operation (70% Q_N) due to the impact of the high flow disorder and non-periodic instabilities in the tip zone. In addition, a noticeable fluctuation of the vortex has been observed along its trajectory as a consequence of the significant interaction with the stator wakes.

This interaction is also manifested on the generation of the tip flow, prior to the formation and swirl of the tip vortex. The evolution of the clearance flow, both in its mean-time distribution or in its unsteady evolution clocked with the vanes passing period, has shown that the leakage flow is also shifted towards the leading edge as the working flow is reduced, fluctuating with the periodicity induced by the stator wakes. The velocity profiles in the tip gap have been obtained and their averaged values computed resulting in typical leakage flows in the order of a 12.4% for the nominal case, 11.3% for partial load and only 6.7% for conditions close to near-stall. In addition, it has been quantified that the fluctuations of these flows with respect to their average values are around 2.8% for nominal conditions and 3.4% for partial load, due to the effect of the rotor-stator interaction in both cases. At 70% Q_N, an overestimated 33.6% for conditions with significant detached flow revealed the influence of the instabilities and turbulence of the flow in the rotor passages, rather than potential periodic interactions of the stator flow. A rotor-only model has been also employed to visualize the differences in the streamwise evolution of the TLF in the absence of inlet guide vanes. In that case, the tip vortex is shown to present very reduced fluctuations at nominal conditions, but on the contrary, the mean-time tip leakage flow is enlarged from 12.4 to 14.5%.

Finally, the analysis of the generation of turbulent kinetic energy in the tip clearance has shown results that are consistent with the formation of the tip flow. They were found to be maximum in those places where the pressure difference between the blade surfaces induces a high-velocity jet, responsible for local detached flow and loss generation. Also, significant periodic fluctuations have been observed on this variable, induced by the stator wakes in the relative frame, which have been quantified as 25% by the effect of the rotor-stator interaction. With respect to the deterministic kinetic energy, it was observed that its presence in the tip is confined close to the leading edge, with typical values at least one order of magnitude lower than the TKE. This is consistent with the previous estimations of the oscillating tip leakage flow in the order of a 3% for stable working conditions.

ACKNOWLEDGEMENTS

The authors gratefully acknowledge the financial support from Project ENE2017-89965-P provided by the Spanish Ministry of Economy, Industry and Competitiveness. Additionally, previous financial support from the Research Project, “Characterization of Aerodynamic Noise due to the Interaction between the Rotor Blades and the Guide Vanes in Axial Flow Fans” (DPI-2006-15720) is also acknowledged.

REFERENCES

Aktürk, A. and Camci, C. (2010), "Axial Flow Fan Tip Leakage Flow Control Using Tip Platform Extensions", *Journal of Fluids Engineering*, Vol. 132, pp. 051109-1–10.

Arnone, A., Marconcini, M., Greco, A.S.D. and Spano, E. (2004), "Numerical investigation of three-dimensional clocking effects in a low-pressure turbine", *Journal of Turbomachinery*, Vol. 126 No. 3, pp. 375-384.

Bae, J.W., Breuer, K.S. and Tan, C.S. (2005), "Active control of tip clearance flow in axial compressors", *Journal of Turbomachinery*, Vol. 127, pp. 352-362.

Basson, A. and Lakshminarayana, B. (1995), "Numerical simulation of tip clearance effects in turbomachinery", *Journal of Turbomachinery*, Vol. 117, pp. 348-359.

Borello, D., Hanjalic, K. and Rispolli, F. (2007), "Computation of tip-leakage flow in a linear compressor cascade with a second-order momentum turbulence closure". *International Journal of Heat and Fluid Flow*, Vol. 28, pp. 587-601.

Corsini, A., Rispoli, F. and Sheard, A.G. (2010), "Shaping of tip end-plate to control leakage vortex swirl in axial flow fans". *Journal of Turbomachinery,* Vol. 132, pp. 031005.

Denton, J.D. (1993), "Loss Mechanisms in Turbomachines". *Journal of Turbomachinery*, Vol. 115, pp. 621-656.

Fernández Oro, J.M., Argüelles Díaz, K.M., Santolaria Morros, C. and Blanco Marigorta, E. (2007), "Unsteady flow and wake transport in a low-speed axial fan with inlet guide vanes". *Journal of Fluids Engineering*, Vol. 129, pp. 1015-1029.

Fernández Oro, J.M., Argüelles Díaz, K.M., Santolaria Morros, C. and Blanco Marigorta, E. (2007), "On the structure of turbulence in a low-speed axial fan with inlet guide vanes". *Experimental Thermal and Fluid Science*, Vol. 32 No. 1, pp. 316-331.

Fernández Oro, J.M., Argüelles Díaz, K.M., Santolaria Morros, C. and Blanco Marigorta, E. (2008), "Analysis of the deterministic unsteady flow in a low-speed axial fan with inlet guide vanes". *Journal of Fluids Engineering*, Vol. 130, 031101, pp. 1-12.

Fernández Oro, J.M., Argüelles Díaz, K.M., Santolaria Morros, C. and Ballesteros-Tajadura, R. (2009), "Impact of the tip vortex on the passage flow structures of a jet fan with symmetric blades". *Proc. IMechE, Part A – Journal of Power and Energy*, Vol. 223 No. 2, pp. 141-155.

Fernández Oro, J.M., Argüelles Díaz, K.M., Santolaria Morros, C. and Galdo Vega, M. (2011), "Numerical simulation of the unsteady stator-rotor interaction in a low-speed axial fan including experimental validation", *International Journal of Numerical Methods for Heat & Fluid Flow*, Vol. 21 No. 2, pp. 168-197.

Fernández Oro, J.M., Meana-Fernández, A., Galdo Vega, M., Pereiras García, B. and González-Pérez, J. (2019), "LES-based simulation of the time-resolved flow for rotor-stator interactions in axial fan stages", *International Journal of Numerical Methods for Heat & Fluid Flow*, Vol. 29 No. 2, pp. 657-681.

Hah, C., Hathaway, M., Katz, J. and Tan, D. (2015), "Investigation of unsteady tip clearance flow in a low-speed one and half stage axial compressor with LES and PIV", *Proceedings of the 2015 ASME-JSME-KSME Joint Fluids Engineering Conference*, AJKFluids2015-2061, 26-31 July, Seoul, Korea.

Inoue, M. and Furukawa, M. (2002), "Physics of tip clearance flow in turbomachinery". *Proceedings of the 2002 ASME Fluids Engineering Division Summer Meeting*, FEDSM2002-31184, 14-18 July, Montreal, Canada.

Jang, C.M., Sato, D., and Fukano, T. (2005), "Experimental analysis on tip leakage and wake flow in an axial flow fan according to flow rates". *Journal of Fluids Engineering*, Vol. 127, 322-329.

Jin, G.-Y., Ouyang, H., Wu, Y.-D. and Du, Z.H. (2011), "An experimental study of the unsteady characteristics of tip-leakage flow of axial fans with circumferential skewed blades at off-design conditions", *Proc. IMechE, Part A – Journal of Power and Energy*, Vol. 225, pp. 802-816.

Jung, J.H. and Joo, W.-G. (2018), "Effect of tip clearance, winglets, and shroud height on the tip leakage in axial flow fans", *International Journal of Refrigeration*, Vol. 93, pp. 195-204.

Lakshminarayana, B., Zaccaria, M. and Marathe, B. (1995), "The structure of tip clearance flow in axial flow compressor", *Journal of Turbomachinery*, Vol. 117, pp. 336-347.

Lee, G.H., Baek, J.H. and Myung, H.J. (2003), "Structure of Tip Leakage Flow in a Forward-Swept Axial-Flow Fan", *Flow, Turbulence and Combustion*, Vol. 70, pp. 241–165.

Lee, H., Park, K. and Choi, H. (2019), "Experimental investigation of tip-leakage flow in an axial flow fan at various flow rates", *Journal of Mechanical Science and Technology*, Vol. 33 No. 3, pp. 1271-1278.

Mao, X., Liu, B. and Zhao, H. (2019), "Effects of tip clearance size on the unsteady flow behaviors and performance in a counter-rotating axial flow compressor", *Proc. IMechE Part G: Journal of Aerospace Engineering*, Vol. 233 No. 3, pp. 1-12.

Miorini, R.L., Wu, H. and Katz, J. (2012), "The Internal Structure of the Tip Leakage Vortex Within the Rotor of an Axial Waterjet Pump", *Journal of Turbomachinery*, Vol. 134, pp. 031018-1–12.

Moghadam, S.M.A., Meinke, M. and Schröder, W. (2019), "Analysis of tip-leakage flow in an axial fan at varying tip-gap sizes and operating conditions", *Computers & Fluids*, Vol. 183, pp. 107-129.

Park, K., Choi, H., Choi, S. and Sa, Y. (2019), “Effect of a casing fence on the tip-leakage flow of an axial flow fan”, *International Journal of Heat and Fluid Flow*, Vol. 77, pp. 157-170.

Pogorelov, A., Meinke, M. and Schröder, W. (2016), “Effects of tip-gap width on the flow field in an axial fan”, *International Journal of Heat and Fluid Flow*, Vol. 61, pp. 466-481.

Sheard, A.G., Corsini, A. and Bianchi, S. (2011), “Stall Warning in a Low-Speed Axial Fan by Visualization of Sound Signals”, *Journal of Engineering for Gas Turbines and Power*, Vol. 133, pp. 041606-1–10.

Storer, J.A. and Cumptsy, N.A. (1991), “Tip leakage flow in axial compressors”, *Journal of Turbomachinery*, Vol. 113, pp. 252-259.

Tan, C.S. (2005), “Unsteady flows in compressors” in *Effects of aerodynamic unsteadiness in axial turbomachines”.* Von Kàrman Institute Lecture Series.

Uzol, O., Brzozowski, D., Chow, Y.-C., Katz, J., and Meneveau, C. (2007), “A database of PIV measurements within a turbomachinery stage and sample comparisons with unsteady RANS”, *Journal of Turbulence*, Vol. 8 No. 10, pp. 1-25.

Van Zante, D.E., Strasizar, A.J., Wood, J.R., Hathaway, M.D. and Okiishi, T.H. (2000), “Recommendations for achieving accurate numerical simulation of tip clearance flows in transonic compressor rotors”. *ASME Journal of Turbomachinery*, Vol. 122, pp. 733-742.

Venter, S. and Kröger, D. (1992), “The effect of tip clearance on the performance of an axial flow fan”. *Energy, Conversion and Management*, Vol. 33 No. 2, pp. 89-97.

Ye, X., Zhang, J. and Li, C. (2017), “Effect of blade tip pattern on performance of a twin-stage variable-pitch axial fan”. *Energy*, Vol. 126, pp. 535-563.

Zhang, D., Shi, W., Van Esch, B.P.M., Shi, L. and Dubuisson, M. (2015), “Numerical and experimental investigation of tip leakage vortex trajectory and dynamics in an axial flow pump”. *Computers & Fluids*, Vol. 112, pp. 61-71.

Zhu, X., Lin, W. and Du, Z. (2005), “Experimental and numerical investigation of the flow field in the tip region of an axial ventilation fan”. *Journal of Fluids Engineering,* Vol. 127, pp. 299-307.